RADIATION RESEARCH **189**, 466–476 (2018)
0033-7587/18 $15.00

DOI: 10.1667/RR14825.1

Dose-Rate Effects in Breaking DNA Strands by Short Pulses of Extreme Ultraviolet Radiation

Luděk Vyšín,[a,e,1] Tomáš Burian,[a,c,d] Egor Ukraintsev,[a] Marie Davídková,[b] Michael E. Grisham,[f] Scott Heinbuch,[f] Jorge J. Rocca[f] and Libor Juha[a,c]

[a] *Institute of Physics,* [b] *Nuclear Physics Institute;* [c] *Institute of Plasma Physics and* [a] *J. Heyrovský Institute of Physical Chemistry, Czech Academy of Sciences, Prague, Czech Republic;* [e] *Department of Nuclear Chemistry, Czech Technical University in Prague, Prague, Czech Republic; and* [f] *Department of Electrical and Computer Engineering, Colorado State University, Fort Collins, Colorado*

Vyšín, L., Burian, T., Ukraintsev, E., Davídková, M., Grisham, M. E., Heinbuch, S., Rocca, J. J. and Juha, L. Dose-Rate Effects in Breaking DNA Strands by Short Pulses of Extreme Ultraviolet Radiation. *Radiat. Res.* 189, 466–476 (2018).

In this study, we examined dose-rate effects on strand break formation in plasmid DNA induced by pulsed extreme ultraviolet (XUV) radiation. Dose delivered to the target molecule was controlled by attenuating the incident photon flux using aluminum filters as well as by changing the DNA/buffer-salt ratio in the irradiated sample. Irradiated samples were examined using agarose gel electrophoresis. Yields of single- and double-strand breaks (SSBs and DSBs) were determined as a function of the incident photon fluence. In addition, electrophoresis also revealed DNA cross-linking. Damaged DNA was inspected by means of atomic force microscopy (AFM). Both SSB and DSB yields decreased with dose rate increase. Quantum yields of SSBs at the highest photon fluence were comparable to yields of DSBs found after synchrotron irradiation. The average SSB/DSB ratio decreased only slightly at elevated dose rates. In conclusion, complex and/or clustered damages other than cross-links do not appear to be induced under the radiation conditions applied in this study.

INTRODUCTION

In the field of radiation chemistry, it is well known that the change in the dose rate, at which ionizing radiation is delivered to the studied (irradiated) system, can affect the yield (radiation chemical yield) of the reactive species (radicals). In irradiated systems where radical-substrate and radical-radical reactions occur and the yields of products of such reactions are different, the radiation chemical yield of the product exhibits a dose-rate dependence. A similar effect is observed with the interaction of high-linear energy transfer (LET) radiation. The radical concentration in the track of the ionizing particle is high and therefore their recombination reactions are favored as they have very high-rate constants (*1*).

During the last decades, numerous sources delivering ionizing radiation to the sample in short and ultra-short pulses were developed and used for various radiation experiments, making it possible to study dose-rate effects more extensively.

Recent progress in the development of ion accelerators using intense laser beam has enabled employment of such sources as compact and cost-effective tools for radiotherapy. The applications and properties are nicely reviewed by Bulanov *et al.* (*2*) and the possible therapeutic advantages discussed by Wilson *et al.* and Ledingham *et al.* (*3, 4*). A perspective on laser-accelerated helium (He) nuclei and its role in radiation therapy has also been discussed elsewhere (*5*). Laser-driven ion accelerations have an inherent property of delivering the ion bunch to the target material in a so-called ultra-high-dose-rate regimen. The proton/ion bunch is created and subsequently accelerated by interaction of an intense femtosecond laser pulse with a thin solid target. When such a bunch is delivered to an appropriate target the rate of energy deposition can reach $>10^9$ Gy/s (*6, 7*) of magnitude in the irradiated material.

Efforts have already been made to demonstrate the capability of laser-accelerated fast ion (proton) bunches to induce DNA lesions in HeLa cells (*6, 8*), A549 pulmonary adenocarcinoma cells (*9*), human FaDu tumors (*10*) or V79 cells (*7*), but no significant difference in relative biological effectiveness (RBE) when compared to conventional accelerators was found. Other researchers, who have utilized laser-based X-ray plasma sources that allowed delivery of energy with a dose rate of 10^{10}–10^{13} Gy/s to irradiate cells under various conditions, came to the same conclusions (*11–13*).

To actually infer how such ultra-high-dose-rate radiation can contribute to DNA damage, it is necessary to study the

[1] Address for correspondence: Institute of Physics of the CAS, Radiation and Chemical Physics, Na Slovance 2, Prague, Czech Republic 18221; email: vysin@fzu.cz.

interaction process on a molecular level, prior to cell, tissue and organ level.

Interaction of energetic particles in matter is accompanied by the release of secondary electrons along its path. These secondary electrons can have a very broad energy spread ranging from approximately one-half of the initial particle energy down to several electronvolts. The distribution of secondary electrons in the target material is governed mainly by an oscillator strength of its constituents. For water and DNA, the most probable energy loss of charged particles peaks at 23 eV (*14*). If it is assumed that the ionization potential of water and DNA is at 12.6 eV (*15*) and ~7 eV (*16*), respectively, it can be inferred that the most probable secondary electron energy lies between 13–16 eV, as estimated elsewhere (*17*). That is, the photoelectron produced by a single photon of the extreme ultraviolet (XUV)-laser radiation can mitigate a most abundant secondary electron produced during an interaction of energetic charged particles, as reported elsewhere (*14, 17*).

A spatiotemporal concept of ionizing radiation energy deposition processes can also be effectively studied by interaction of intense XUV and soft X-ray (SXR) radiation since the energies carried by the photons (10–500 eV) are comparable to the secondary electron energies, which are liberated in track structures called ''spurs'' and ''blobs''. Spurs and blobs are generated by ionizing radiation when energy imparted to secondary electrons is less than 100 eV and 100–500 eV, respectively (*18*).

The interaction process of XUV and SXR with matter is almost exclusively driven by the photoelectric effect such that a high-intensity beam of photons is converted to electrons in a very well-defined way. The low-energy radiation (XUV) has a very short attenuation length of approximately a few nanometers in almost any material so it creates a very high density of ionizations and excitations in the irradiated material. The study of spur overlap phenomena could benefit from that.

In the current work, we have focused on an interaction of XUV radiation with a photon energy of 26.4 eV, delivered by table-top capillary discharge laser, with plasmid DNA in varying dose-rate regimens. Single- and double-strand breaks (SSBs and DSBs) were observed in irradiated thin layers of plasmid DNA after agarose gel electrophoresis separation. Dose rate was adjusted by changing the ratio of buffer salt (Tris and EDTA) to plasmid DNA in the sample, as well as by attenuating the laser beam. The beam was delivered in a pulsed regimen with single pulse duration of 1.5 ns (FWHM). In addition, we investigated the inter-duplex cross-link (*CL*) formation observed after irradiation by means of atomic force microscopy (AFM).

Supercoiled plasmid DNA, such as pBR322, serves as a widely used model of a DNA molecule in DNA damage studies using various types of ionizing radiation including protons (*19–21*), heavy ions (*22–24*), gamma radiation (*25–27*) and low-energy electrons (*28–30*). It was also very effectively used in a study of radical scavenging reactions (*31, 32*). Its advantage is that irradiated and subsequently isolated plasmid molecules are not subjected to cell repair mechanisms, thus providing a good substrate for further investigation and damage quantification *ex situ*.

MATERIALS AND METHODS

Samples of stock plasmid DNA solution (pBR322; New England Biolabs Inc., Ipswitch, MA) stored in 1× TE buffer (10 m*M* Tris-HCl, 1 m*M* EDTA, pH 7.5) were spectrophotometrically checked for concentration. Ratio of absorbance at 260 and 280 nm yielded a value of 937 ng/μl. This stock solution was diluted to a working solution with a concentration of 30 ng/μl, with 1× TE buffer (Sigma-Aldrich® LLC, Steinheim, Germany) and deionized water, to three sets of solutions. The TE buffer concentration was chosen based on desired dose rate. The working solution was then checked for the fraction of the supercoiled form, which was determined to be 97%. No linear or cross-link plasmid conformation was present in the control sample. The amount of DNA in each sample was 150 ng. A droplet of 5-μl solution was pipetted onto a glass coverslip and left under nitrogen atmosphere to evaporate at room temperature. The prepared DNA thin films were then irradiated in a vacuum chamber evacuated down to $\sim 10^{-4}$ mbar. Details on the XUV laser source are discussed elsewhere (*33, 34*), as are the details on the interaction setup of plasmid irradiation (*35*). Since the transverse electromagnetic profile of the capillary-discharge laser beam exhibits a ''donut'' shape, samples were placed at the position where intensity reaches its maximum (Fig. 1). For each irradiated sample, a control sample was also placed in the vacuum chamber but not irradiated. Exposures of all samples to the vacuum was no longer than 30 min during both irradiation and control experiments.

Buffer Concentration Measurement

The concentration of the TE buffer in stock samples was verified by means of the EDTA detection method developed by Wang *et al*. (*36*). This method utilizes detection of excess Fe^{3+} ions, which were not chelated by the EDTA in the solution, reduced by Na_2SO_3 and with a subsequent color complex detection at 510 nm after addition of the phenanthroline monohydrate. For this study, the reaction volume was reduced to 100 μl and the final volume was detected using a Nano Stick (Scinco, Seoul, Korea) micro cuvette designed to detect samples in volumes as low as 5 μl. Final TE concentrations were confirmed to be 1× TE (10 m*M* Tris and 1 m*M* EDTA), 0.1× TE (1 m*M* Tris and 0.1 m*M* EDTA) and 0.04× TE (0.4 m*M* Tris and 0.04 m*M* EDTA).

Strand Break Detection

Irradiated samples were washed off the glass substrate by 10 μl of 1× TE buffer. Prior to agarose gel electrophoresis assay, 2 μl of 6× Loading Dye (Thermo Scientific, Darmstadt, Germany) were added to each sample. Samples were then loaded into 1% agarose gel (molecular biology grade, SERVA, Heidelberg, Germany) which was prestained with SYBR® Green I (Sigma-Aldrich) fluorescent dye. The samples were allowed to migrate for 60 min at 5 V/cm electric field intensity in 0.5× TAE (20 m*M* Tris, 1 m*M* acetic acid, 0.5 m*M* EDTA, pH 8.4) buffer. The gels were photographed on a transilluminator table (UVItec Ltd., Cambridge, UK) behind a Wratten no. 15 filter and then integrated using ImageJ version 1.48 image processing software (NIH, Bethesda, MD) (*37*).

AFM Measurement

To prepare the samples of the cross-linked DNA plasmids for an AFM measurement, bands containing the cross-linked DNA were cut out and the DNA was extracted using a High Pure PCR Purification Kit (Roche Diagnostics, Mannheim, Germany). For AFM scanning,

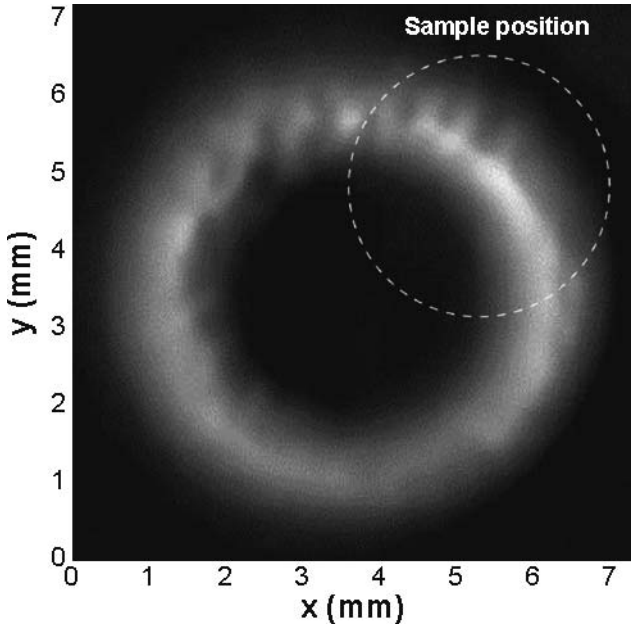

FIG. 1. Transverse electromagnetic mode of the capillary discharge laser beam captured at the sample position by CMOS chip covered with a phosphor scintillator shielded with a 150-nm aluminum filter. The dashed circle represents the sample size and position in the beam. Total intensity over the sample is 25% of the beam intensity.

10-μl droplets of 1–10 ng/μl DNA solution in 20 m*M* $MgCl_2$ and 150 m*M* NaCl were pipetted on freshly cleaved mica samples. After 10 min of adhesion DNA solution was removed using a deionized water stream and nitrogen flow. DNA samples were studied in air on an ICON AFM (Bruker, Coventry, UK) in PFQNM mode using CF_4 plasma-treated Multi75Al cantilevers (*38*). The force threshold in PFQNM mode was approximately 0.2–2 nN. Scanned areas ranged from 1×1 μm to 5×5 μm, mostly $1{,}024 \times 1{,}024$ lines. Scan speed was 0.1–0.15 Hz.

Photon Fluence Measurement

An average photon fluence (hereafter referred to as ''photon fluence'') in a single pulse was measured using a silicon photodiode XUV-100 (OSI Optoelectronics, Hawthorne, CA). The quantum efficiency of 3.2 electrons per photon at the energy of the XUV photon (26.4 eV) was determined by spline-interpolating the data provided by the manufacturer. To control the photon fluence on the sample per pulse, thin aluminum filters (Lebow Corp., Goleta, CA) of various thickness were inserted into the beam path. Transmission of each filter was measured by recording the photodiode signal and calculating the ratio of the values measured with and without the filter. The thickness of all the filters as well as their transmissions are summarized in the Table 1. A photon fluence at the sample position was calculated by taking the fraction of the annular beam profile covering the area of the sample, which was placed at the position of maximum intensity, see Fig. 1. The fraction of the beam intensity over the sample was determined to be 0.25 of the net intensity according to the geometry of the irradiation setup.

TABLE 1
Aluminum Filter Used, Filter Transmissions and Corresponding Photon and Energy Fluence

Filter thickness (nm)	Transmission T_{filter}	Photon fluence ϕ (photons m^{-2})	Energy fluence ϕ (J m^{-2})
No filter	100.0%	1.8×10^{16}	7.7×10^{-2}
1×100	61.9%	1.1×10^{16}	4.8×10^{-2}
2×100	38.3%	7.0×10^{15}	3.0×10^{-2}
2×150	29.6%	5.4×10^{15}	2.3×10^{-2}
3×100	23.7%	4.3×10^{15}	1.8×10^{-2}

Data Fitting

Measured DNA fractions as a function of the photon fluence were fitted using the method introduced by McMahon and Currell (*39*). However, this method had to be modified to allow for the fact that the XUV radiation is strongly absorbed in a very thin layer of the irradiated material, thus exhibiting the effect of saturation observed previously by others (*35, 40*). This phenomenon has been corrected for by inserting a dimensionless parameter *f*, which represents the fraction of the plasmid DNA in the sample that is not affected by the radiation (*41*). The changes in DNA forms of supercoiled (*S*), closed circular (*C*) and linear (*L*) as functions of the incident average photon fluence ϕ can be described by the following system of differential equations:

$$\frac{dS(\phi)}{d(\phi)} = -(\beta_S + \beta_D)(S(\phi) - S_0 f), \tag{1}$$

$$\frac{dC(\phi)}{d(\phi)} = \beta_S(S(\phi) - S_0 f) - \beta_D(C(\phi) - C_0 f) - \eta\beta_S^2\,\phi[S(\phi) + C(\phi) - (S_0 + C_0)f], \tag{2}$$

$$\frac{dL(\phi)}{d(\phi)} = \beta_D(S(\phi) - S_0 f) + \beta_D(C(\phi) - C_0 f) + \eta\beta_S^2\,\phi[S(\phi) + C(\phi) - (S_0 + C_0]f. \tag{3}$$

The variables β_S and β_D represent the probabilities for single SSB and DSB induction in one plasmid molecule per photon per m^2, respectively, assuming Poisson distribution of the hit events, S_0, is the initial fraction of supercoiled form in the sample and η is the probability parameter describing induction of one DSB from two adjacent SSBs at opposite strands in certain distances of base pairs (bp) ($\eta = 10/4{,}361$) for pBR322, i.e., 10 bp distance). Integration of Eqs. (1–3) yields:

$$S(\phi) = S_0(1 - f)\exp[-(\beta_S + \beta_D)\phi] + S_0 f, \tag{4}$$

$$C(\phi) = (C_0 + S_0)(1 - f)\exp\left(-\beta_D\phi - \frac{1}{2}\beta_S^2\eta\phi^2\right) - S_0(1 - f)\exp[-(\beta_S + \beta_D)\phi] + C_0 f, \tag{5}$$

$$(\phi) = (C_0 + S_0)(1 - f)\left[1 - exp\left(-\beta_D\phi - \frac{1}{2}\beta_S^2\eta\phi^2\right)\right] + L_0, \tag{6}$$

where C_0 and L_0 are the initial fractions of closed circular and linear forms of plasmid DNA.

Dose Estimation and Radiation Chemical Yield

The energy absorbed in the DNA-buffer salt of each sample was estimated based on the value of the fitted parameters, β_S and β_D, obtained by fitting the photon fluence response curve. Reciprocal value of β_S and β_D yields the photon fluence that was absorbed to induce single SSB or DSB, respectively. The dose (Gy) required to induce a single SSB or DSB in one plasmid molecule was calculated according to the relationship:

$$D_{SSB,\text{DSB}} = \frac{26.4 \cdot 1.602 \times 10^{-19}}{\beta_{S,D} \cdot \sigma_S}\left[1 - \exp(-(\tau/\rho)_S\sigma_S)\right], \tag{7}$$

where σ_S in kg/m^2 is the surface density of the sample, $(\tau/\rho)_S$ is the

TABLE 2
DNA Sample Parameters According to the Composition

Tris-HCl/EDTA concentration	σ_{sample} (kg/m^2)	w_{pBR322}
0.04×	7.63×10^{-5}	0.330
0.1×	1.34×10^{-4}	0.164
1×	1.00×10^{-3}	0.019

mass photoabsorption coefficient of the sample and the numerical values are a conversion of the photon energy from electronvolts to joules. This simple formula is based on the assumption that the sample is homogeneous and that all of the values of the f parameter were found to be less than 1, thus suggesting full absorption of the beam in the sample. The surface density of the sample was equal to the mass of the sample (DNA and TE buffer salts present) divided by its area of 3.4 ± 0.1 mm. The concentration of the DNA, which was measured spectrophotometrically against the buffer with specific TE concentrations, was converted to mass according to the total volume deposited on the coverslip. The mass of the TE buffer salt was calculated from the known concentration (*42*), stoichiometric composition: $C_{5.0}H_{12.4}N_{1.2}O_{3.8}Na_{0.3}Cl_{0.5}$, and deposited volume assuming full water evaporation. Mass photoabsorption coefficient was calculated according to Henke *et al*. (*43*), For plasmid DNA, it has also been considered that, even under vacuum conditions, with zero relative humidity, there remain 2.5 residual water molecules ($\Gamma = 2.5$) per nucleotide attached to the sugar phosphate backbone (*44, 45*). TE buffer salt concentrations, surface densities and mass fractions of plasmid DNA in three different combinations are shown in Table 2. The composite mass attenuation coefficient of the sample was calculated as a weighted sum of the mass photoabsorption coefficients of both constituents.

The mass photoelectric absorption coefficient of the plasmid DNA was determined by converting the optical data acquired by Inagaki (*46*), considering the same optical properties of both calf thymus and pBR322 DNA. The conversion used was the same as that used by Hieda *et al*. (*47*):

$$(\tau/\rho)_{pBR322^{(\lambda)}} = \frac{\sigma_{abs}}{m_{pBR322}} = \frac{4 \cdot \pi \cdot \kappa(\lambda)}{\lambda \cdot \rho}, \qquad (8)$$

where σ_{abs} is the absorption cross-section, m_{pBR322} is the plasmid molecule mass and $\kappa(\lambda)$ is the extinction coefficient, i.e., imaginary part of the complex refraction index as a function of the wavelength λ and ρ is the DNA density of 1,350 kg/m^3. Further information on the derivation of Eq. (8) can be found in ref. (*48*). For this purpose, data used from the published article by Inagaki (*46*) were interpolated to correspond to the wavelength of 46.9 nm (26.4 eV).

Radiation chemical yield (G value) of SSB or DSB (expressed in nmol/J), was estimated from the dose (Gy) and the plasmid mass m_{pBR322} (kg) as:

$$G_{SSB,DSB} = \frac{10^9}{D_{SSB,DSB} \cdot N_A \cdot m_{pBR322}}, \qquad (9)$$

where N_A is the Avogadro constant. The plasmid mass was taken, including the structural water, to be 5.11×10^{-21} kg.

RESULTS

Cross-Link Detection

When the DNA was irradiated without any filter and in the lowest salt content (0.04× TE), a slow-migrating peak corresponding to a band containing cross-linked DNA was observed, as previously reported elsewhere (*40, 49, 50*). Cross-link bands induced by XUV 26.4-eV radiation are apparent in the gel image in Fig. 2. An important observation is that the cross-link bands are being detected along with the linear form as the absorbed photon fluence is increased.

AFM measurements were performed to elucidate the nature of the cross-linked DNA molecules and to refine the fitted parameters for SSB and DSB yields. Since a significant fraction (almost 10% at the maximum dose per pulse, 1,213.6 Gy/pulse) of plasmid DNA is converted into the cross-linked form it was necessary to determine which form of the plasmid DNA was actually represented by the band. The *CL* form most likely originates from a cross-linking between the most abundant DNA forms present: i.e., *S* and *C* or *C-C* interduplex, as suggested by work of Luo *et al*. (*49*). The other bands related to the cross-link between two supercoiled forms, *S-S*, were not detected in the current work.

Figure 3A shows long linear fragments of plasmid DNA molecules obtained by AFM scanning on one sample after immobilization of 1 ng/μl concentrated extract. Figure 3B represents the first stage of aggregation of short linear fragments (*51, 52*) from the same extract. Figure 3C shows a typical representation of a large clustered plasmid DNA molecular structure. Figure 3D demonstrates that DNA molecules can form a 1.3 nm thick layer (*53*). Figures 3E and 2F show that at higher concentration of DNA (10 ng/μl) molecules can form net structures on a mica surface. Figure

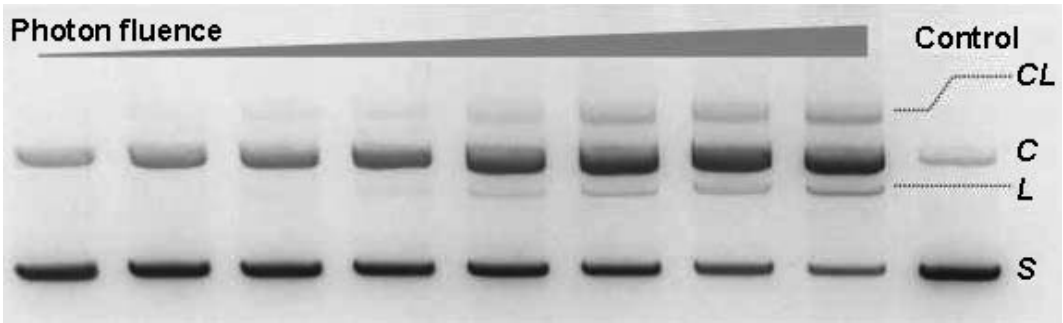

FIG. 2. Plasmid DNA forms separated in an agarose gel irradiated without a filter in the lowest TE buffer concentration (0.04×). Bands correspond to the fraction of plasmid DNA forms; from the top: cross-links (*CL*), closed-circular (*C*), linear (*L*) and supercoiled (*S*).

TABLE 3
Selected Parameters for pBR322 Irradiated by 26.4-eV Photons with Highest Photon Fluence (No Aluminum Filter Inserted) with Various Buffer Salt to DNA Ratios

	Cross-section ($\times 10^{-19}$ m^2)							
	Action			Quantum yield		G value (nmol/J)		
Tris-HCl/EDTA concentration	SSB	DSB	Absorption	SSB	DSB	SSB	DSB	SSB/DSB
0.04×	4.15	0.18	2,419	1.7×10^{-3}	7.5×10^{-5}	2.01	0.088	22.7
0.1×	3.58	0.08	2,419	1.5×10^{-3}	3.4×10^{-5}	3.68	0.056	65.5
1×	3.18	0.03	2,419	1.3×10^{-3}	1.1×10^{-5}	22.2	0.176	125.6

2E represents a magnified section of Fig. 2F. In general, all scanned samples extracted from the *CL* band of the gel resemble linear interconnected structures. Figures 3G and 2H show DNA molecules on a mica from 1 ng/μl solution extracted from the band corresponding to the supercoiled (*S*) form of the DNA. As the DNA is precipitated with isopropanol during the extraction procedure it forms compact clusters, which were subsequently identified. The compact ''clumps'' represent the condensed supercoiled plasmids. This finding also correlates with very low fluorescence of all the samples that were extracted and repooled to the stained agarose gel to check the consistency of the extraction method. The observed low fluorescence is probably caused by the poor intercalation of the fluorescence probe to the condensed double helix of large fraction of *S*, *C* and *L* or *CL* forms.

We conclude from the AFM measurements that, in our case, the integrated values of *CL* peaks represent mainly the *L* form and therefore can be added to the linear fraction of each sample for subsequent evaluation.

DNA Breakage

Figure 4 shows a typical dose-response curve where the integrated fractions of the *S*, *R* and *L* forms of the plasmid DNA are plotted as a function of the entrance photon fluence (and dose) along with the fitted functions $S(\phi)$, $C(\phi)$ and $L(\phi)$. From irradiated samples containing different buffer salt/plasmid DNA ratios, it can be seen that the penetration depth of the XUV radiation is increased as the composition of the sample is more diluted, i.e., is less shielded by the TE buffer residuals. This dependence is clearly visible in Fig. 5, where we plotted the fraction of the supercoiled form for all three sample compositions as a function of the entrance photon fluence. It is evident that as the composition of the sample is more diluted [contains lower ratio (w/w) of buffer salts to DNA] the photons can penetrate deeper into the sample material, converting more supercoiled forms to circular and linear forms and, as a result, decreasing the value of the *f* parameter. The shielded fraction of the *S* form is simply the *f* parameter multiplied by the fraction of the initial supercoiled form, S_0. The shielding effect was observed also in the formation of cross-links. When the buffer salt/plasmid DNA ratio (w/w) was maintained at the lowest level (2:1), we detected a fraction of cross-links that was approximately the same as for DSBs. When the buffer salt/plasmid DNA ratio was raised to 5:1 and finally to 50:1 there were only DNA forms corresponding to SSBs and DSBs, and no cross-links were detected.

When the values of the *f* parameter are plotted as a function of the dose rate, they decrease almost logarithmically, as shown in Fig. 6. For the highest photon fluence and the sample composition with the buffer salt/plasmid DNA ratio of 2:1 (w/w) (highest dose rate), the shielded fraction was approximately 0.2 and increased to 0.6 where the buffer salt/plasmid DNA ratio reached maximum value of 50:1. This trend was also observed for all samples with the same buffer salt/plasmid DNA ratios (w/w). Figure 6 shows that as the dose rate is increased the shielded fraction reaches a limit value (~0.15). This suggests that the dominant process for observing the saturation effect is indeed the attenuation length, which is dependent on the sample composition. We add that an even lower buffer salt/plasmid DNA ratio is experimentally very difficult to achieve, since dialysis is required to lower the salt concentration in the solution. Without the supporting buffer salts, plasmid DNA layers become very fragile, and the supercoiled form is very unstable when dried and placed in a low-pressure environment (*54*).

Action Cross-Section

Action cross-sections for induction of SSBs and DSBs have been taken as the reciprocals of the fitted values of β_S and β_D, respectively. The quantum yield, i.e., the number of strand breaks produced per absorbed photon, was determined by dividing the experimental action cross-section for SSB or DSB induction by the absorption cross-section. The absorption cross-section data for the pBR322 plasmid molecule was determined by multiplying the mass photoelectric absorption coefficient by its mass. Table 3 summaries action cross-sections, as well as quantum and radiation chemical yields, of SSBs and DSBs induced in three different compositions irradiated with the highest photon fluence, i.e., no filter inserted. These data were compared to the available values from other researchers (*55–57*) and plotted in Fig. 7.

DISCUSSION

Ionization processes in the solvation shell of the DNA molecule can result in a formation of the $OH^{\bullet}$ radical, which

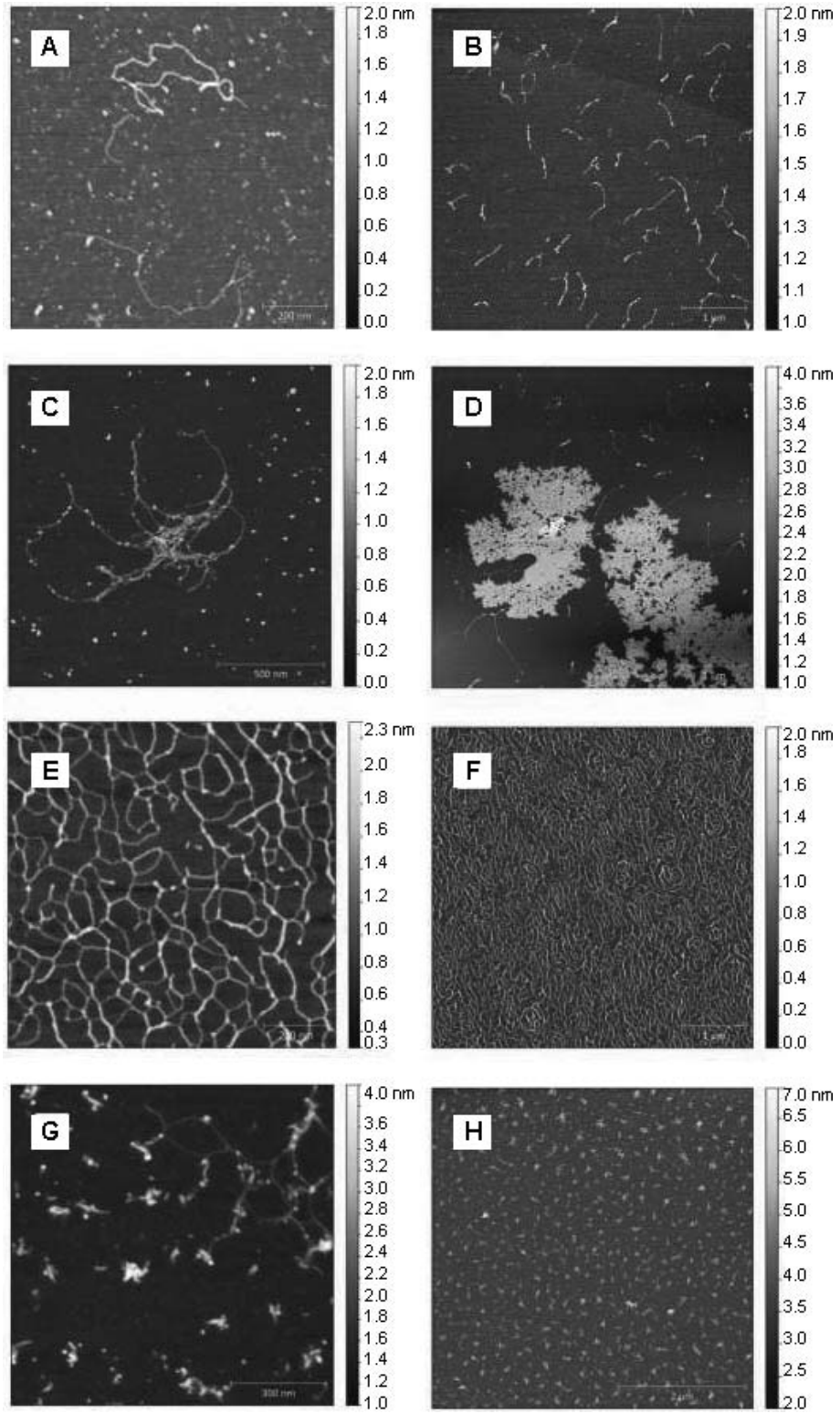

FIG. 3. Panels A–D: DNA molecules deposited on mica from 1 ng/μl solution. Panels E–F: DNA molecules deposited on mica from 10 ng/μl solution, both DNA solutions extracted from the gel corresponding to the cross-link (*CL*) form of the DNA; panel E shows a magnified section of panel F. Panels G–H: DNA molecules on a mica from 1 ng/μl solution extracted from the band corresponding to the supercoiled (*S*) form of the DNA. All samples received the maximum dose during irradiation. Samples were cut from the respective bands of the gel.

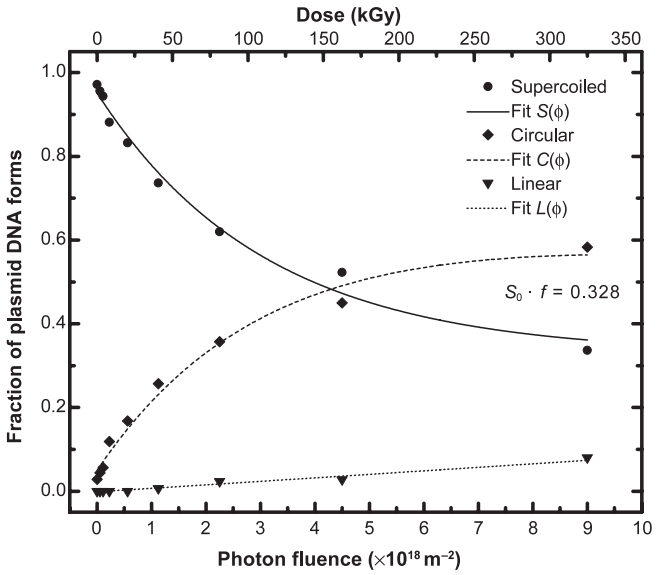

FIG. 4. Fractions of pBR322 plasmid forms dissolved in 0.1× TE buffer irradiated as a function of a photon fluence behind a 100-nm Al filter. Measured points are fitted using the sets of Eqs. (4–6).

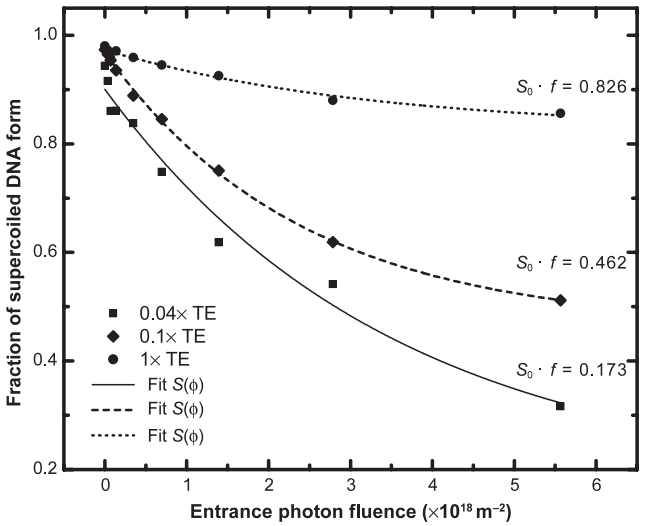

FIG. 5. Fraction of supercoiled form of pBR322 plasmid dissolved in different concentrations of TE buffer irradiated by same number of photons behind two 100-nm aluminum filters. Values of $S_0 \cdot f$ represent the nonirradiated fraction of the sample.

can either react with the nucleobase by addition resulting in a modified base, or can abstract hydrogen from the sugar phosphate backbone, resulting in an abasic (Ab) site or strand breakage. It has been reported that ionization events in tightly-bound water molecules ($\Gamma < 9$) result in a transfer of the hole and excess electron to the DNA molecule (*25, 58–60*). The process of the hole transfer to the DNA molecule together with the direct ionization process in the DNA has been identified in the literature as the direct-type effect (*60*), since they are indistinguishable without using time-resolved techniques.

The damage after the direct-type effect should be different from the indirect effect. Holes transferred to the DNA can end on the bases, predominantly on guanine, since it has the lowest ionization potential, preventing the DNA from strand breakage by ultimately forming easily-repaired 8-oxo-G (*62*); conversely, the transferred holes can end on the sugar phosphate backbone resulting in sugar cation radicals, which has been reported as a precursor to strand breaks (*63, 64*). All the strand breaks are not caused by the sugar radicals formed. For example, the G values of SSBs in DNA ($\Gamma = 22$) irradiated with X rays revealed that all trapped and converted sugar radicals form up to 43% of the total SSBs detected (*65*). Therefore, other mechanisms must play an important role in the strand breakage process associated with direct-type effects.

Excess electrons from direct-type ionization events are either captured by the bases with the highest electron affinity (i.e., cytosine and thymine) or added to the sugar phosphate backbone via dissociative electron attachment resulting into strand breaks (*62*). The latter process is typical for low-energy electrons (LEEs) with an energy range of up to 20 eV (*29, 66, 67*). It has been shown that LEEs with energies below 15 eV cause a prominent resonant peak in SSB and DSB yield functions with a strong maximum near 10 eV (*28, 29*). Experiments conducted with a higher-incident electron energy resolution in the range of 0–4 eV also revealed strong peaks at 0.8 and 2.2 eV for SSB induction, but none for DSB formation (*68*). The chain scission caused by electrons in such an energy range can be explained by the formation of the transient negative ions of DNA subunits, i.e., resonant attachment of LEEs to either a base or the sugar phosphate backbone (*69*). Such a transient molecular anion can decay by releasing the base, dissociating the base into smaller products, or the electron can be transferred to the antibonding σ* orbital of the C-O bond on the sugar phosphate backbone resulting into the chain scission. This scheme is believed to be one of the main

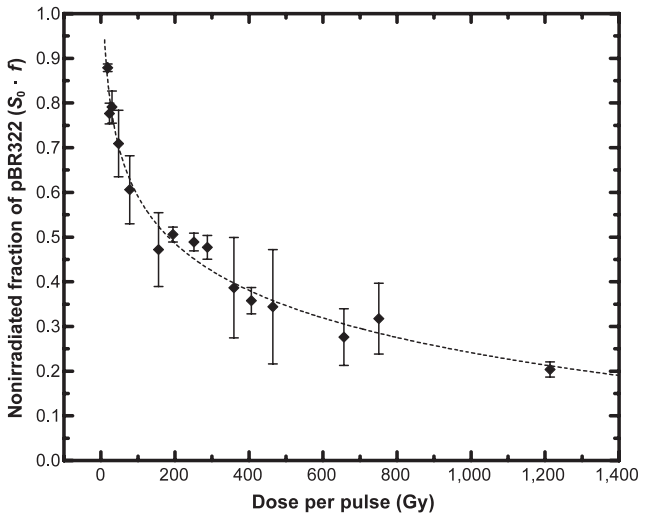

FIG. 6. Shielded fraction ($S_0 \cdot f$) as a function of the dose per pulse (dose rate). The dashed line serves as a visual guide.

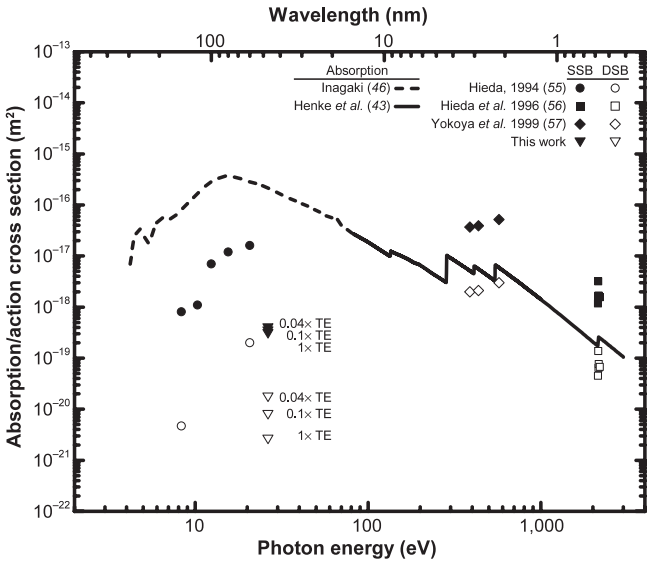

FIG. 7. Absorption/action cross-section for the pBR322 plasmid DNA irradiated with 26.4-eV photons with different weight fraction of buffer salt, in perspective with other action cross-sections reported in other studies using synchrotron radiation.

mechanisms for the strand break formation induced by LEEs in DNA (*70*).

Since the photoelectric effect dominates the radiation-matter interaction in the XUV spectral range, photoelectrons released in the sample by an absorption of the XUV laser photons have a low energy and a very narrow energy distribution. This is caused by the ionization limit of the DNA in 7.5–10 eV (*16*) and monochromaticity of the XUV laser radiation. After collisions with sample constituents, the photoelectron energies would not exceed 19 eV. This means that a part of photoelectrons could collisionally ionize the matter, providing some secondary electrons. However, the ionization ''cascade'' will be undeveloped because of the strictly limited electron energy. Thus, the limited energy distribution of electrons ensures that every electron deposits its energy within the DNA molecule itself because of their few-nanometer-scale range (*14, 71*). It is therefore highly probable that LEEs play an important role in the observed strand breakage mechanism.

It has been reported that a deprotonation at the C4′ position on the sugar leads to strand break formation with aldehyde groups formed at the 3′ end of the strand (*63, 64*). This electrophilic aldehyde is capable of generating covalent adduct to the nucleophilic base on the opposing strand (*72, 73*), resulting in an intra-strand cross-link. The Ab sites, as shown above, are also susceptible to inter-strand linkage with guanine or adenine bases (*74, 75*). This process is likely responsible for the observed cross-linking.

Table 4 provides a summary of results from other studies in which plasmid DNA undergoes synchrotron irradiation with similar photon energy as that emitted by the XUV capillary-discharge laser. The composition of the samples varied among these studies, but the mass ratio of the plasmid DNA in the sample was reported to be greater than 0.9 in all cases. As shown in Table 4, the quantum yield for a given energy, (only the given energy was provided in most cases), is in the range of 3.7×10^{-2} to 8.1×10^{-2} for SSB induction and 6.3×10^{-4} to 3.9×10^{-3} for DSBs.

We compared our results to other studies using synchrotron XUV photons. In our study, the quantum yields of SSB induction for pulsed high-dose-rate XUV radiation are in the order of 10^{-3} strand breaks per absorbed photon (Table 3). This value does not change significantly with different sample compositions used in the case of low-energy photon irradiation and, compared to other studies, is almost of the same order of magnitude as quantum yields of DSB induction using synchrotron radiation (data shown in Table 4).

One reason for the higher quantum yields observed in the case of synchrotron radiation is the much lower dose rate at which the energy was deposited to the sample. This observation can be explained by the fast delivery of the XUV photons in a single XUV laser pulse. They are deposited in times shorter than 1.5 nanosecond. The fast delivery and very strong absorption of XUV radiation in a relatively small volume results in a very high density of ionizations/excitations. Therefore, the peak concentration of the holes and low-energy electrons can reach an enormous value. However, the concentration jump not only increases the probability of a reaction of such transient species with a target (here, DNA and its subunits), but also favors mutual

TABLE 4
Comparison of the Results Obtained for Similar Photon Energies as the Capillary Discharge Laser in Studies Performed Using Synchrotron Radiation

			Quantum yield		G value (nmol/J)		
Ref.	System	Photon energy (eV)	SSB	DSB	SSB	DSB	SSB/DSB
(*54*)	pBR322	20.7	4.9×10^{-2}	6.3×10^{-4}	25.0	0.3	80.0
(*73*)[a]	pBR322	25.0	8.1×10^{-2}	3.9×10^{-3}	33.5	1.6	20.8
(*74*)[a]	pMSG-CAT	25.0	4.5×10^{-2}	9.2×10^{-4}	18.6	0.4	49.0
(*75*)[b]	pMSG-CAT	25.0	3.7×10^{-2}	8.9×10^{-4}	15.4	0.4	41.6
(*76*)[a]	pMSG-CAT	25.0	6.3×10^{-2}	1.6×10^{-3}	25.9	0.7	40.0

[a] Data were estimated based on the given energy, and only the given energy was provided in this reference.
[b] Personal communication (K. Prise).

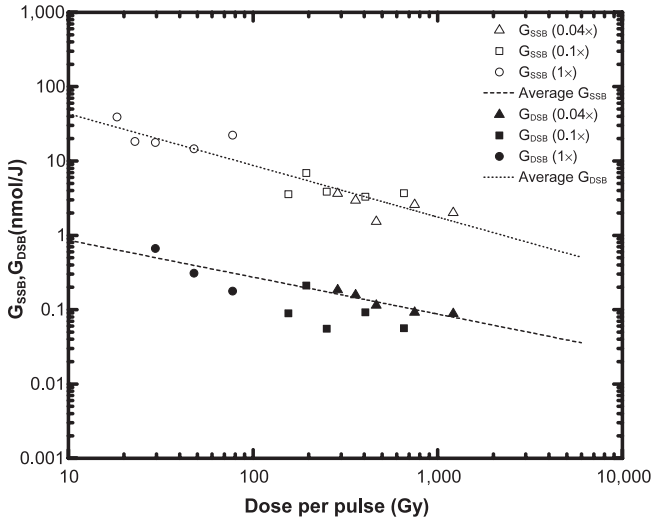

FIG. 8. Yields of SSBs and DSBs, expressed in nmol J^{-1}, as a function of the dose per pulse. The dotted and dashed lines are the average values of the SSB and DSB yields, respectively.

reactions between the transients, resulting in electron-hole recombinations.

The ratio of average SSBs to DSBs in our study has an overall decreasing trend as a function of the dose per pulse. As the average dose per pulse is increased from 18.3 to 1,213.6 Gy, which corresponds to a dose rate of 1.2×10^{10} and 8.1×10^{11} Gy/s, respectively, the ratio of average SSBs to DSBs drops from 58.1 to 25.3. Trends of the average G values for SSBs and DSBs are shown in Fig. 8, where the average G values for SSBs and DSBs are marked by dotted and dashed lines, respectively. The dose-rate effects occur from a competition between electron-hole recombination and radical formation processes. If we assume that the recombination probability drops for lower dose rates, then a higher fraction of sugar cation radicals can be converted into SSBs under these conditions. This is consistent with the dependence as measured and shown in Fig. 8.

Cross-linking is more prevalent when the DNA is irradiated in the absence of oxygen, as reported by Lett and Alexander (*76*). They also suggested that the cross-linking process is mainly due to the direct effect of ionizing radiation. This notion, and the observation that cross-links were detected only in samples with the lowest salt/DNA ratio (2:1), may support the hypothesis that it is indeed the action of the directly absorbed radiation, i.e., the result of ionization and excitation events. There is also the important factor of the high packing density of DNA in the thin films. This was suggested by Purkayastha *et al*. (*65*) as an explanation of the measured higher yields of free radicals in DNA thin films. The detected cross-links and measured radiation chemical yields indicate that direct-type processes are underlying strand break induction and are sensitive to the rate at which the energy is being deposited.

The quantum yield values obtained in our study and those obtained for LEEs are not easily comparable. It is evident that part of the interaction must be governed by the excess electrons from the ionization events. The only indicator that can yield a fraction of the LEE interaction process involved is the SSB/DSB ratio. The SSB/DSB ratio results in this study are of the order of tens of SSBs per single DSB compared to 2:8 in the case of LEE irradiation (*28, 29*). This suggests that almost ten times more SSBs can be attributed to the hole transfer to the sugar phosphate backbone in the case of XUV irradiation.

CONCLUSION

We have demonstrated the action of pulsed intense XUV (26.4 eV) laser radiation on the induction of SSBs and DSBs in a plasmid DNA. The radiation was delivered in pulses with duration of 1.5 nanosecond, thereby reaching very high dose rates of up to 8.1×10^{11} Gy/s. Our values of SSB quantum yields are of the same order of magnitude as DSB quantum yields reported in studies using synchrotron radiation. Those findings suggest that the energy deposition process of XUV is indeed dependent on the rate at which the energy is being deposited. Calculated radiation chemical yields exhibit a clear dose-rate dependence. The induction of cross-links appears to be unrelated to the direct-type effect of ionizing radiation only, but might be related to a more complicated behavior of electrons and holes created by XUV photons in the solvation shell of the DNA.

ACKNOWLEDGMENTS

This work was supported by the Czech Science Foundation (grant no. GA 13-28721S) and Laserlab Europe (grant no. 654148, Horizon 2020 - The EU Framework Programme for Research and Innovation). We are grateful for the FAIR and FAIR.CZ collaboratives for their support of networking in this research stream. The Colorado State University researchers acknowledge the support of U.S. Department of Energy, Office of Science, Basic Energy Sciences (award no. DE-FG02-04ER15592). MD and EU acknowledge financial support provided by the Czech Science Foundation (grant no. P108/12/G108). We thank Mrs. Lenka Černíková for providing the gel extraction kit as well as vital recommendations.

Received: May 3, 2017; accepted: January 30, 2018; published online: March 5, 2018

REFERENCES

1. Spinks JWT, Woods RJ. An introduction to radiation chemistry. 2nd ed. New York, Toronto: John Wiley and Sons; 1976.
2. Bulanov SV, Wilkens JJ, Esirkepov TZ, Korn G, Kraft G, Kraft SD, et al. Laser ion acceleration for hadron therapy. Physics-Uspekhi 2014; 57:1149–79.
3. Wilson P, Jones B, Yokoi T, Hill M, Vojnovic B. Revisiting the ultra-high dose rate effect: implications for charged particle radiotherapy using protons and light ions. Br J Radiol 2012; 85:e933–9.
4. Ledingham K, Bolton P, Shikazono N, Ma C-M. Towards laser driven hadron cancer radiotherapy: a review of progress. Appl Sci 2014; 4:402–43.
5. Bulanov SS, Esarey E, Schroeder CB, Leemans WP, Bulanov SV, Margarone D, et al. Helium-3 and helium-4 acceleration by high

power laser pulses for hadron therapy. Phys Rev Spec Accel Beams 2015; 18:61302–1-061302–6.

6. Bin J, Allinger K, Assmann W, Dollinger G, Drexler GA, Friedl AA, et al. A laser-driven nanosecond proton source for radiobiological studies. Appl Phys Lett 2012; 101:243701–1–4.
7. Doria D, Kakolee KF, Kar S, Litt SK, Fiorini F, Ahmed H, et al. Biological effectiveness on live cells of laser driven protons at dose rates exceeding 10(9) Gy/s. AIP Adv 2012; 2:11209.
8. Auer S, Hable V, Greubel C, Drexler G, Schmid TE, Belka C, et al. Survival of tumor cells after proton irradiation with ultra-high dose rates. Radiat Oncol 2011; 6:139.
9. Yogo A, Maeda T, Hori T, Sakaki H, Ogura K, Nishiuchi M, et al. Measurement of relative biological effectiveness of protons in human cancer cells using a laser-driven quasimonoenergetic proton beamline. Appl Phys Lett 2011; 98:53701.
10. Zlobinskaya O, Siebenwirth C, Greubel C, Hable V, Hertenberger R, Humble N, et al. The effects of ultra-high dose rate proton irradiation on growth delay in the treatment of human tumor xenografts in nude mice. Radiat Res 2014; 181:177–83.
11. Tillman C, Grafström G, Jonsson A-C, Jonsson B-A, Mercer I, Mattsson S, et al. Survival of mammalian cells exposed to ultrahigh dose rates from a laser-produced plasma X-ray source. Radiology 1999; 213:860–5.
12. Hill MA, Stevens DL, Marsden SJ, Allott R, Turcu ICE, Goodhead DT. Is the increased relative biological effectiveness of high LET particles due to spatial or temporal effects? Characterization and OER in v79-4 cells. Phys Med Biol 2002; 47:3543–55.
13. Shinohara K, Nakano H, Miyazaki N, Tago M, Kodama R. Effects of single-pulse ($\leq$1 ps) X-rays from laser-produced plasmas on mammalian cells. J Radiat Res 2004; 45:509–14.
14. LaVerne JA, Pimblott SM. Electron energy-loss distributions in solid, dry DNA. Radiat Res 1995; 141:208.
15. Banna MS, McQuaide BH, Malutzki R, Schmidt V. The photoelectron spectrum of water in the 30 to 140 eV photon energy range. J Chem Phys 1986; 84:4739–44.
16. Colson AO, Besler B, Sevilla MD. Ab initio molecular orbital calculations on DNA base pair radical ions: effect of base pairing on proton-transfer energies, electron affinities, and ionization potentials. J Phys Chem 1992; 96:9787–94.
17. Pimblott SM, LaVerne JA. Production of low-energy electrons by ionizing radiation. Radiat Phys Chem 2007; 76:1244–7.
18. Mozumder A, Magee JL. Model of tracks of ionizing radiations for radical reaction mechanisms. Radiat Res 1966; 28:203–14.
19. Vysin L, Pachnerova Brabcova K, Stepan V, Moretto-Capelle P, Bugler B, Legube G, et al. Proton-induced direct and indirect damage of plasmid DNA. Radiat Environ Biophys 2015; 54:343–52.
20. Leloup C, Garty G, Assaf G, Cristovao A, Breskin A, Chechik R, et al. Evaluation of lesion clustering in irradiated plasmid DNA. Int J Radiat Biol 2005; 81:41–54.
21. Sui L, Wang Y, Wang X, Kong F, Liu J, Zhou P. Clustered DNA damage induced by protons radiation in plasmid DNA. Chinese Sci Bull 2013; 58:3217–23.
22. Pachnerova Brabcova K, Sihver L, Yasuda N, Matuo Y, Stepan V, Davidkova M. Clustered DNA damage on subcellular level: effect of scavengers. Radiat Environ Biophys 2014; 53:705–12.
23. Terato H, Tanaka R, Nakaarai Y, Nohara T, Doi Y, Iwai S, et al. Quantitative analysis of isolated and clustered DNA damage induced by gamma-rays, carbon ion beams, and iron ion beams. J Radiat Res 2008; 49:133–46.
24. Urushibara A, Shikazono N, O'Neill P, Fujii K, Wada S, Yokoya A. LET dependence of the yield of single-, double-strand breaks and base lesions in fully hydrated plasmid DNA films by 4He(2+) ion irradiation. Int J Radiat Biol 2008; 84:23–33.
25. Yokoya A, Cunniffe SMT, O'Neill P. Effect of hydration on the induction of strand breaks and base lesions in plasmid DNA films by gamma-radiation. J Am Chem Soc 2002; 124:8859–66.
26. Shao C, Saito M, Yu Z. Formation of single- and double-strand breaks of pBR322 plasmid irradiated in the presence of scavengers. Radiat Environ Biophys 1999; 38:105–9.
27. Milian FM, Gouveia AN, Gual MR, Echeimberg JO, Arruda-Neto JDT, Garcia F, et al. In vitro effects of gamma radiation from (60)Co and (137)Cs on plasmid DNA. J Biol Phys 2007; 33:155–60.
28. Huels MA, Boudaïffa B, Cloutier P, Hunting D, Sanche L. Single, double, and multiple double strand breaks induced in DNA by 3–100 eV electrons. J Am Chem Soc 2003; 125:4467–77.
29. Boudaïffa B, Cloutier P, Hunting D, Huels MA, Sanche L. Resonant formation of DNA strand breaks by low-energy (3 to 20 eV) electrons. Science 2000; 287:1658–60.
30. Alizadeh E, Sanche L. Induction of strand breaks in DNA films by low energy electrons and soft X-ray under nitrous oxide atmosphere. Radiat Phys Chem 2012; 81:33–9.
31. Milligan JR, Aguilera JA, Ward JF. Variation of single-strand break yield with scavenger concentration for the SV40 minichromosome irradiated in aqueous solution. Radiat Res 1993; 133:158–62.
32. Fulford J, Bonner P, Goodhead D, Hill M, O'Neill P. Experimental determination of the dependence of OH radical yield on photon energy: a comparison with theoretical simulations. J Phys Chem A 1999; 103:11345–9.
33. Heinbuch S, Grisham M, Martz D, Rocca JJ. Demonstration of a desk-top size high repetition rate soft X-ray laser. Opt Express 2005; 13:4050.
34. Vysin L, Burian T, Chalupsky J, Grisham M, Hajkova V, Heinbuch S, et al. Characterization of focused beam of desktop 10-Hz capillary-discharge 46.9-nm laser. Proc. SPIE 7361, Damage to VUV, EUV, and X-Ray Optics II, 73610O. 2009.
35. Novakova E, Vysin L, Burian T, Juha L, Davidkova M, Mucka V, et al. Breaking DNA strands by extreme-ultraviolet laser pulses in vacuum. Phys Rev E 2015; 91:42718–1–8.
36. Wang J, Yu J, Kong XZ, Hou L. Spectrophotometric determination of EDTA in aqueous solution through ferroin formation using sodium sulfite as the reducer. Chemosphere 2013; 91:351–7.
37. Schneider CA, Rasband WS, Eliceiri KW. NIH image to ImageJ: 25 years of image analysis. Nat Methods 2012; 9:671–5.
38. Rezek B, Ukraintsev E, Kratka M, Taylor A, Fendrych F, Mandys V. Epithelial cell morphology and adhesion on diamond films deposited and chemically modified by plasma processes. Biointerphases 2014; 9:31012–1–8.
39. McMahon SJ, Currell FJ. A robust curve-fitting procedure for the analysis of plasmid DNA strand break data from gel electrophoresis. Radiat Res 2011; 175:797–805.
40. Folkard M, Prise KM, Vojnovic B, Davies S, Roper MJ, Michael BD. Measurement of DNA damage by electrons with energies between 25 and 4000 eV. Int J Radiat Biol 1993; 64:651–8.
41. Wyer JA, Butterworth KT, Hirst DG, Latimer CJ, Montenegro EC, Shah MB, et al. Fragmentation and plasmid strand breaks in pure and gold-doped DNA irradiated by beams of fast hydrogen atoms. Phys Med Biol 2009; 54:4705–21.
42. Sambrook J, Russell DW, Maniatis T. Molecular cloning: a laboratory manual. 2nd ed. Cold Spring Harbor, New York: Cold Spring Harbor Laboratory Press; 1989.
43. Henke BL, Gullikson EM, Davis JC. X-ray interactions: photoabsorption, scattering, transmission, and reflection at E = 50–30,000 eV, Z = 1–92. At Data Nucl Data Tables 1993; 54:181–342.
44. Tao NJ, Lindsay SM, Rupprecht A. Structure of DNA hydration shells studied by Raman spectroscopy. Biopolymers 1989; 28:1019–30.
45. Swarts SG, Sevilla MD, Becker D, Tokar CJ, Wheeler KT. Radiation-induced DNA damage as a function of hydration: I. Release of unaltered bases. Radiat Res 1992; 129:333–44.

46. Inagaki T. Optical and dielectric properties of DNA in the extreme ultraviolet. J Chem Phys 1974; 61:4246–50.

47. Hieda K, Hayakawa Y, Ito A, Kobayashi K, Ito T. Wavelength dependence of the formation of single-strand breaks and base changes in DNA by the ultraviolet radiation above 150 nm. Photochem Photobiol 1986; 44:379–83.

48. Attwood D. Wave propagation and refractive index at EUV and soft X-ray wavelengths. In: Soft X-rays and extreme ultraviolet radiation. New York: Cambridge University Press; 2007. p. 55–64.

49. Luo X, Zheng Y, Sanche L. DNA strand breaks and crosslinks induced by transient anions in the range 2–20 eV. J Chem Phys 2014; 140:155101–1–11.

50. Cai Z, Cloutier P, Hunting D, Sanche L. Comparison between X-ray photon and secondary electron damage to DNA in vacuum. J Phys Chem B 2005; 109:4796–800.

51. Cary RB, Peterson SR, Wang J, Bear DG, Bradbury EM, Chen DJ. DNA looping by Ku and the DNA-dependent protein kinase. Proc Natl Acad Sci U S A 1997; 94:4267–72.

52. Tian Y, He Y, Ribbe AE, Mao C. Preparation of branched structures with long DNA duplex arms. Org Biomol Chem 2006; 4:3404.

53. Garibotti A V., Perez-Rentero S, Eritja R. Functionalization and self-assembly of DNA bidimensional arrays. Int J Mol Sci 2011; 12:5641–51.

54. Smialek MA, Balog R, Jones NC, Field D, Mason NJ. Preparation of DNA films for studies under vacuum conditions. Eur Phys J D 2010; 60:31–6.

55. Hieda K. DNA damage induced by vacuum and soft X-ray photons from synchrotron radiation. Int J Radiat Biol 1994; 66:561–7.

56. Hieda K, Hirono T, Azami A, Suzuki M, Furusawa Y, Maezawa H, et al. Single- and double-strand breaks in pBR322 plasmid DNA by monochromatic X-rays on and off the K-absorption peak of phosphorus. Int J Radiat Biol 1996; 70:437–45.

57. Yokoya A, Watanabe R, Hara T. Single- and double-strand breaks in solid pBR322 DNA induced by ultrasoft X-rays at photon energies of 388, 435 and 573 eV. J Radiat Res 1999; 40:145–58.

58. Becker D, Sevilla MD. The chemical consequence of radiation damage to DNA. In: Lett JT, Sinclair WK, editors. Advances in radiation biology, Vol 17. San Diego: Academic Press; 1993. p. 121–80.

59. LaVere T, Becker D, Sevilla M. Yields of $^{\bullet}$OH in gamma-irradiated DNA as a function of DNA hydration: hole transfer in competition with $^{\bullet}$OH formation. Radiat Res 1996; 145:673–80.

60. Debije MG, Strickler MD, Bernhard W. On the efficiency of hole and electron transfer from the hydration layer to DNA: an EPR study of crystalline DNA X-irradiated at 4 K. Radiat Res 2000; 154:163–70.

61. Bernhard WA. Radical reaction pathways initiated by direct energy deposition in DNA by ionizing radiation. In: Greenberg MM, editor. Radical and radical ion reactivity in nucleic acid chemistry. Hoboken, NJ: John Wiley and Sons; 2009. p. 41–68.

62. Adhikary A, Becker D, Sevilla MD. Electron spin resonance of radicals in irradiated DNA. In: Lund A, Shiotani M, editors. Applications of EPR in radiation research. Cham: Springer International Publishing; 2014. p. 629–63.

63. Adhikary A, Collins S, Khanduri D, Sevilla MD. Sugar radicals formed by photoexcitation of guanine cation radical in oligonucleotides. J Phys Chem B 2007; 111:7415–21.

64. Khanduri D, Adhikary A, Sevilla MD. Highly oxidizing excited states of one-electron-oxidized guanine in DNA: wavelength and pH dependence. J Am Chem Soc 2011; 133:4527–37.

65. Purkayastha S, Milligan JK, Bernhard WA. Correlation of free radical yields with strand break yields produced in plasmid DNA by the direct effect of ionizing radiation. J Phys Chem B. 2005; 109:16967–73.

66. Dugal PC, Huels MA, Sanche L. Low-energy (5–25 eV) electron damage to homo-oligonucleotides. Radiat Res. 1999; 151:325–33.

67. Kumar A, Sevilla MD. Low-energy electron (LEE)-induced DNA damage: theoretical approaches to modeling experiment. In: Handbook of computational chemistry. Dordrecht: Springer Netherlands; 2012. p. 1215–56.

68. Martin F, Burrow PD, Cai Z, Cloutier P, Hunting D, Sanche L. DNA strand breaks induced by 0–4 eV electrons: the role of shape resonances. Phys Rev Lett 2004; 93:68101.

69. Sanche L. Biological chemistry: Beyond radical thinking. Nature 2009; 461:358–9.

70. Sanche L. Low energy electron interaction with DNA: bond dissociation and formation of transient anions, radicals and radical anions. In: Greenberg MM, editor. Radical and radical ion reactivity in nucleic acid chemistry. Hoboken, NJ: John Wiley and Sons; 2009. p. 239–93.

71. Cole A. Absorption of 20-eV to 50,000–eV electron beams in air and plastic. Radiat Res 1969; 38:7–33.

72. Regulus P, Duroux B, Bayle P-A, Favier A, Cadet J, Ravanat J-L. Oxidation of the sugar moiety of DNA by ionizing radiation or bleomycin could induce the formation of a cluster DNA lesion. Proc Natl Acad Sci U S A 2007; 104:14032–7.

73. Cadet J, Wagner JR. DNA base damage by reactive oxygen species, oxidizing agents, and UV radiation. Cold Spring Harb Perspect Biol 2013; 5:a012559.

74. Price NE, Johnson KM, Wang J, Fekry MI, Wang Y, Gates KS. Interstrand DNA-DNA cross-link formation between adenine residues and abasic sites in duplex DNA. J Am Chem Soc 2014; 136:3483–90.

75. Price NE, Catalano MJ, Liu S, Wang Y, Gates KS. Chemical and structural characterization of interstrand cross-links formed between abasic sites and adenine residues in duplex DNA. Nucleic Acids Res 2015; 43:3434–41.

76. Lett JT, Alexander P. Crosslinking and degradation of deoxyribonucleic acid gels with varying water contents when irradiated with electrons. Radiat Res 1961; 15:159–73.